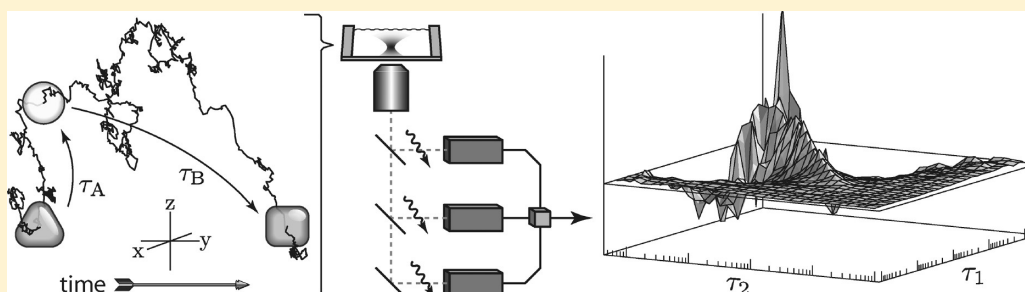


The Spectroscopic Basis of Fluorescence Triple Correlation Spectroscopy

William K. Ridgeway,^{†,‡} David P. Millar,[†] and James R. Williamson^{*,†,‡}

[†]Department of Molecular Biology and [‡]Department of Chemistry and The Skaggs Institute for Chemical Biology, The Scripps Research Institute, 10550 North Torrey Pines Road, La Jolla, California 92037, United States

S Supporting Information



ABSTRACT: We have developed fluorescence triple correlation spectroscopy (F3CS) as an extension of the widely used fluorescence microscopy technique fluorescence correlation spectroscopy. F3CS correlates three signals at once and provides additional capabilities for the study of systems with complex stoichiometry, kinetic processes, and irreversible reactions. A general theory of F3CS was developed to describe the interplay of molecular dynamics and microscope optics, leading to an analytical function to predict experimental triple correlations of molecules that freely diffuse through the tight focus of the microscope. Experimental correlations were calculated from raw fluorescence data using triple correlation integrals that extend multiple-tau correlation theory to delay times in two dimensions. The quality of experimental data was improved by tuning specific spectroscopic parameters and employing multiple independent detectors to minimize optoelectronic artifacts. Experiments with the reversible system of freely diffusing 16S rRNA revealed that triple correlation functions contain symmetries predicted from time-reversal arguments. Irreversible systems are shown to break these symmetries, and correlation strategies were developed to detect time-reversal asymmetries in a comprehensive way with respect to two delay times, each spanning many orders of magnitude in time. The correlation strategies, experimental approaches, and theory developed here enable studies of the composition and dynamics of complex systems using F3CS.

INTRODUCTION

When a small collection (1–100) of freely diffusing fluorescent molecules are observed, the fluorescence intensity vs time data contain large fluctuations arising from sources such as diffusion, chemical reactions, fast photophysics, and conformational rearrangements in engineered FRET constructs. Analyzing these fluctuations reveals a wide variety of microscopic rates, without the need to physically perturb the sample or remove it from equilibrium. High-quality fluctuation data are readily obtained using microscopes constructed for single-molecule detection, and recent growth of single-molecule biophysics has renewed interest in statistical methods for analyzing fluorescence fluctuations to complement true single-molecule experiments.

There are two basic approaches to analyze fluorescence fluctuations. Histograms of average photon count rates, or of higher moments or cumulants, are fit to models that take into account the joint probability distributions associated with focal volume occupancy and photon emission.^{1–7} This allows mixtures containing molecules of varying brightness to be characterized in terms of concentration and brightness ratios. In

the second approach, fluorescence correlation spectroscopy (FCS),^{8–11} a correlation function, $G(\tau)$ is calculated for a fluorescence intensity time trace $i(t)$ against itself, or against another related intensity^{12,13} at various delay times τ :

$$G(\tau) = \frac{\langle \delta i(t) \delta i(t + \tau) \rangle}{\langle i(t) \rangle^2} \quad (1)$$

$$\langle i(t) \rangle = \frac{1}{T} \sum_{d=1}^T i(t_d)$$

$$\delta i(t) = i(t) - \langle i(t) \rangle$$

Angled brackets indicate ensemble averages approximated by the time averages over all T data points. As with the histogram methods, the amplitudes $G(0)$ at zero delay times are directly related to particle number distributions. The correlation data at

Received: September 6, 2011

Revised: December 22, 2011

Published: January 9, 2012

nonzero delay times contain a wealth of additional kinetic information on processes such as intermolecular folding reactions, fast photophysics, diffusion, and environmental perturbations. Since molecular rate constants are rapidly obtained from a wide variety of nonideal samples with high concentrations of analyte, and even live cells,^{14,15} FCS has been broadly applied to various biochemical problems. Histogram analysis and FCS can be combined to better understand samples undergoing complex reaction–diffusion processes,^{16–18} and complicated particle distributions and kinetic processes are analyzed simultaneously with a second type of FCS, the family of high-order autocorrelations^{19–23}

$$G_{m,n}(\tau) = \frac{\langle \delta I^n(t) \delta I^m(t + \tau) \rangle - \langle \delta I^n(t) \rangle \langle \delta I^m(t) \rangle}{\langle i(t) \rangle^{m+n}} \quad (2)$$

where the exponents m and n are positive nonzero integers.

We are concerned with developing a third type of FCS spectroscopy, fluorescence triple correlation spectroscopy (F3CS), by introducing a third term into the correlation

$$G(\tau_1, \tau_2) = \frac{\langle \delta i(t) \delta i(t + \tau_1) \delta i(t + \tau_2) \rangle}{\langle i(t) \rangle^3} \quad (3)$$

There are diverse applications for F3CS. For example, when three-color detection is used to observe differentially labeled molecules in solution, triple-labeled molecules can be distinguished from a combination of double-labeled particles. In a separate manuscript, we are reporting the joint use of double and triple correlation FCS to quantify a mixture of 10 bacterial ribosome assembly intermediates that differ by subunit stoichiometry. F3CS can be used to identify irreversible systems that violate time-reversal symmetry. While double correlation FCS and high-order autocorrelations with $m = n$ are necessarily symmetric about $\tau = 0$,²⁴ triple correlations are not so restricted and theoretical considerations²⁵ suggest asymmetric triple correlation functions are strong evidence of irreversible systems.

F3CS has been proposed for decades, and progress toward experimental realization has been tantalizing but difficult. High order correlations^{19–22} laid the theoretical foundations for multiple observations, though only identical signals across one delay time. Triple-color coincidence²⁶ combined three colors, though it could not resolve data across delay times. Time-integrated fluorescence cumulant analysis⁷ indirectly considered the statistics of multiple delay times, though it also did not observe triple correlated data directly. Fluorescence from immobilized enzymes²⁷ was analyzed by triple correlation, though using a very limited range of delay times. The first of three tasks addressed here was building upon these foundations and developing the full theory of F3CS. The second task, computing experimental correlation integrals, was arguably the most difficult barrier to achieving F3CS. Finally, experiments were tuned to maximize signal-to-noise, eliminate instrumental artifacts, and search for time-reversal asymmetries. By revisiting the fundamental theory and practice of FCS, F3CS was finally realized experimentally, opening up new possibilities for studying the composition and dynamics of complex systems.

EXPERIMENTAL METHODS

Optics. The optics for triple correlation were well established in the designs of sensitive microscopes for FCS^{28,29} and triple-color coincidence analysis,²⁶ and we have designed and constructed a similar microscope for collection of

F3CS data that is described in detail elsewhere. The microscope was configured to collect single-color data by splitting photons among the three avalanche photodiode (APD) photon detectors (SPCM-AQR-14 and SPCM-AQRH-14, Perkin-Elmer) using neutral density, nonpolarizing beam splitters, and a single bandpass filter (HQ580/60M, Chroma, Brattleboro, VT) was placed upstream of the beam splitters. The microscope was operated with widefield detection by focusing fluorescence onto a fraction of the 170 μm diameter detector heads of APDs.

16S rRNA/Oligo. The 16S rRNA sample was prepared by annealing a 25nt DNA oligo to the 3' terminus of natural 16S rRNA, which was purified from *E. coli* as described.³⁰ Oligo: 5'-Alexa546 -TAA GGA GGT GAT CCA ACC GCA GGT T -3' (Invitrogen, Carlsbad, CA). RNA and DNA were mixed at 20 μM in 10 mM Tris–HCL (pH 8.0), 1 mM EDTA, and 100 mM NaCl and heated to 95 °C for 5 min followed by slow cooling to 30° at $-2^\circ/\text{min}$. The annealed product was gel purified on a 1.2% agarose gel and extracted directly into the buffer used for observation: 80 mM Tris–Hepes (pH 7.6), 20 mM MgCl_2 , 330 mM KCl, 25 $\mu\text{g/mL}$ BSA, 0.5% Tween-20, 500 μM protocatechuic acid, 100 nM protocatechuic-3,4-dioxygenase,³¹ 1.6 mM Trolox, 400 μM Trolox–quinone.³²

Data Acquisition and Software. Data were collected at 18 °C, using femtosecond laser excitation centered at 830 ± 20 nm. Unless noted otherwise, laser powers used were approximately 2 mW less than the power at which saturation effects changed the profile of the FCS spectra. Acquisition time varied by data set, 120–600 s. A comprehensive suite of software (Triple Correlation Toolbox) was written to directly acquire data, calculate experimental correlation functions, and fit data. The suite will be made freely available, alongside details of the data acquisition strategies and exact algorithms presented in a communication.

RESULTS AND DISCUSSION

General Theory of F3CS. FCS correlation integrals are designed to detect finite temporal fluctuations in raw fluorescence intensity data $i(t)$. For generality, the correlation functions are written as cross correlations¹² that detect fluctuations across two or three independent detection channels $i_\alpha(t)$, $i_\beta(t)$, $\{i_\gamma(t)\}$

$$G_{\alpha \times \beta}(\tau) = \frac{\langle \delta i_\alpha(t) \delta i_\beta(t + \tau) \rangle}{\langle i_\alpha(t) \rangle \langle i_\beta(t) \rangle} \quad (4)$$

$$G_{\alpha \times \beta \times \gamma}(\tau_1, \tau_2) = \frac{\langle \delta i_\alpha(t) \delta i_\beta(t + \tau_1) \delta i_\gamma(t + \tau_2) \rangle}{\langle i_\alpha(t) \rangle \langle i_\beta(t) \rangle \langle i_\gamma(t) \rangle} \quad (5)$$

where $G_{\alpha \times \beta}(\tau)$ correlates signals in channels α and β and $G_{\alpha \times \beta \times \gamma}(\tau_1, \tau_2)$ correlates signals in channels α , β , and γ . All channels record reaction and diffusion of the same molecules at the same time, but whether all channels record the same fluorescence or each preferentially records different wavelengths, polarization states, etc., depends on the experiment. Auto correlations of a single channel $i_\alpha(t)$ are obtained by replacing $i_\beta(t)$ and $i_\gamma(t)$ with $i_\alpha(t)$.

It is necessary to predict the form of correlation functions that result from a mixture of molecules diffusing through the tight focus of a microscope. Loosely following the original treatment of Elson and Magde⁹ for double correlations (eq 4), here we predict the equivalent form of the F3CS equation (eq 5)

in order to establish basic relations, highlight assumptions, and provide a foundation for subsequent, more sophisticated theories.

Correlations of a Complex Mixture. The time-varying fluorescence intensity $i_x(t)$ of channel x is the sum of the random background b_x and the fluorescence of the sample integrated over each point in space. The fluorescence intensity is given by the product of the concentration $C_j(\mathbf{r}, t)$ of each of M chemical species j , the intensity of the fluorescence $\varepsilon_{x,j}$, and the point-spread function of the microscope $I(\mathbf{r})$

$$i_x(t) = b_x + \sum_{j=1}^M \varepsilon_{x,j} \int C_j(\mathbf{r}, t) I(\mathbf{r}) d\mathbf{r} \quad (6)$$

The molecular brightness $\varepsilon_{x,j}$ combines all contributions from laser power, dye extinction coefficients, quantum yields, and microscope detection efficiency, which deviates slightly from the notation of Elson and Magde.⁹ The molecular brightness $\varepsilon_{x,j}$ is assumed to be constant, and the only time-dependent quantity

in $i_x(t)$ is $C_j(\mathbf{r}, t)$, which contains the molecular fluctuations of interest. The quantity $C_j(\mathbf{r}, t)$ is assumed to be stationary in time and spatially homogeneous so that a mean concentration \bar{C}_j can be calculated, allowing time-averaged intensity and short-term fluctuations about the mean to be calculated as

$$\langle i_x(t) \rangle = b_x + \sum_{j=1}^M \varepsilon_{x,j} \bar{C}_j \int I(\mathbf{r}) d\mathbf{r} \quad (7)$$

$$\delta i_x(t) = \sum_{j=1}^M \varepsilon_{x,j} \int \delta C_j(\mathbf{r}, t) I(\mathbf{r}) d\mathbf{r} \quad (8)$$

$$\delta C_j(\mathbf{r}, t) = C_j(\mathbf{r}, t) - \bar{C}_j$$

Equations 7 and 8 are directly substituted into eq 5 to obtain a general expression for calculating F3CS curves

$$G_{\alpha \times \beta \times \gamma}(\tau_1, \tau_2) = \frac{\sum_{j,k,l=1}^M \varepsilon_{\alpha,j} \varepsilon_{\beta,k} \varepsilon_{\gamma,l} \iiint I(\mathbf{r}_1) I(\mathbf{r}_2) I(\mathbf{r}_3) \langle \delta C_j(\mathbf{r}_1, t) \delta C_k(\mathbf{r}_2, t + \tau_1) \delta C_l(\mathbf{r}_3, t + \tau_2) \rangle d\mathbf{r}_1 d\mathbf{r}_2 d\mathbf{r}_3}{\langle i_\alpha(t) \rangle \langle i_\beta(t) \rangle \langle i_\gamma(t) \rangle} \quad (9)$$

While the same point-spread function is employed for all three observations, the theory could be expanded to use multiple point-spread functions centered at different locations throughout an image, which is of particular interest as imaging FCS experiments have recently demonstrated the potential to analyze anisotropic diffusion and map compartmentalization in complex cellular structures.³³

The triple sum in the numerator is simplified by assuming that molecules of different species do not diffuse together, and that different species do not interconvert. In this case,

$$\begin{aligned} & \sum_{j,k,l=1}^M \langle \delta C_j(\mathbf{r}_1, t) \delta C_k(\mathbf{r}_2, t + \tau_1) \delta C_l(\mathbf{r}_3, t + \tau_2) \rangle \\ &= \sum_{j,k,l=1}^M \delta_{j,k} \delta_{k,l} \langle \delta C_j(\mathbf{r}_1, t) \delta C_k(\mathbf{r}_2, t + \tau_1) \delta C_l(\mathbf{r}_3, t + \tau_2) \rangle \\ &= \sum_{j=1}^M \langle \delta C_j(\mathbf{r}_1, t) \delta C_j(\mathbf{r}_2, t + \tau_1) \delta C_j(\mathbf{r}_3, t + \tau_2) \rangle \end{aligned} \quad (10)$$

where $\delta_{j,k}$ is the Kronecker delta. Combining eq 9 and eq 10, the multispecies correlation function simplifies to a weighted sum of single-species correlation functions $G_{jjj}(\tau_1, \tau_2)$

$$G_{\alpha \times \beta \times \gamma}(\tau_1, \tau_2) = \frac{\sum_{j=1}^M \varepsilon_{\alpha,j} \varepsilon_{\beta,j} \varepsilon_{\gamma,j} G_{jjj}(\tau_1, \tau_2)}{\langle i_\alpha(t) \rangle \langle i_\beta(t) \rangle \langle i_\gamma(t) \rangle} \quad (11)$$

$$G_{jjj}(\tau_1, \tau_2) = \iiint I(\mathbf{r}_1) I(\mathbf{r}_2) I(\mathbf{r}_3) \times \phi_{jjj}(\mathbf{r}_1, \mathbf{r}_2, \mathbf{r}_3, \tau_1, \tau_2) d\mathbf{r}_1 d\mathbf{r}_2 d\mathbf{r}_3 \quad (12)$$

$$\phi_{jjj}(\mathbf{r}_1, \mathbf{r}_2, \mathbf{r}_3, \tau_1, \tau_2) = \langle \delta C_j(\mathbf{r}_1, t) \delta C_j(\mathbf{r}_2, t + \tau_1) \delta C_j(\mathbf{r}_3, t + \tau_2) \rangle \quad (13)$$

The expression for $G_{jjj}(\tau_1, \tau_2)$ is factored into separate terms for the microscope geometry $I(\mathbf{r})$ and for the triple concentration correlation function $\phi_{jjj}(\mathbf{r}_1, \mathbf{r}_2, \mathbf{r}_3, \tau_1, \tau_2)$. The latter term is agnostic to any optical parameters of the FCS experiment and

contains the physical model of the molecular behavior to be studied.

Solution of the Triple Molecular Correlation Function.

For diffusion, the triple molecular correlation function $\phi_{jjj}(\mathbf{r}_1, \mathbf{r}_2, \mathbf{r}_3, \tau_1, \tau_2)$ reflects the joint probability $P(\mathbf{r}_1, t; \mathbf{r}_2, t + \tau_1; \mathbf{r}_3, t + \tau_2)$ that a molecule initially observed at (position = \mathbf{r}_1 , time = t) will then be observed at ($\mathbf{r}_2, t + \tau_1$) and ($\mathbf{r}_3, t + \tau_2$) (Figure 1).

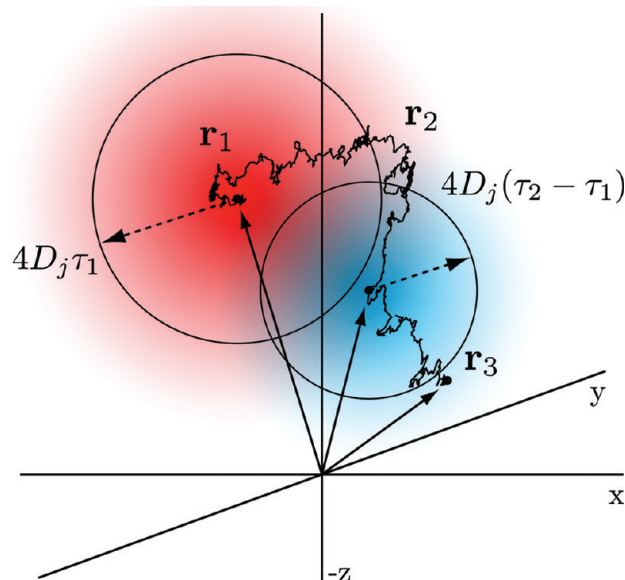


Figure 1. The molecular correlation function $\phi_{jjj}(\mathbf{r}_1, \mathbf{r}_2, \mathbf{r}_3, \tau_1, \tau_2)$ describes the probability that a molecule originally at \mathbf{r}_1 at time t will diffuse to \mathbf{r}_2 at time $t + \tau_1$ and then will diffuse to \mathbf{r}_3 at time $t + \tau_2$.

This can be written in terms of the equilibrium probability $P^e(\mathbf{r}_1, t)$ and two conditional probabilities:

$$\begin{aligned} & P(\mathbf{r}_1, t; \mathbf{r}_2, t + \tau_1; \mathbf{r}_3, t + \tau_2) \\ &= P^e(\mathbf{r}_1, t) P(\mathbf{r}_2, t + \tau_1 | \mathbf{r}_1, t) P(\mathbf{r}_3, t + \tau_2 | \mathbf{r}_2, t + \tau_1; \mathbf{r}_1, t) \end{aligned}$$

As free diffusion is a stationary Markov process, the probabilities are independent of time t and the conditional probability of the third measurement only depends on the state of the system at the time of the second measurement

$$P(\mathbf{r}_3, t + \tau_2 | \mathbf{r}_2, t + \tau_1; \mathbf{r}_1, t) = P(\mathbf{r}_3, \tau_2 - \tau_1 | \mathbf{r}_2, 0)$$

Thus, the joint probability is written in terms of two delay times, τ_1 and $\tau_2 - \tau_1$:

$$\begin{aligned} P(\mathbf{r}_1, t; \mathbf{r}_2, t + \tau_1; \mathbf{r}_3, t + \tau_2) \\ = P^e(\mathbf{r}_1)P(\mathbf{r}_2, \tau_1 | \mathbf{r}_1, 0)P(\mathbf{r}_3, \tau_2 - \tau_1 | \mathbf{r}_2, 0) \end{aligned} \quad (14)$$

As was the case⁹ for the function $\phi_{jj}(\mathbf{r}_1, \mathbf{r}_2, \tau)$, a solution for $\phi_{jjj}(\mathbf{r}_1, \mathbf{r}_2, \mathbf{r}_3, \tau_1, \tau_2)$ is found by calculating the rate at which concentration fluctuations decay. Consistent with eq 14, two decays are sought, one as a function of τ_1 and the other as a function of $\tau_2 - \tau_1$, making use of the diffusion equation and a boundary condition:

$$\frac{\partial \delta C_j(\mathbf{r}, \tau)}{\partial \tau} = D_j \nabla^2 \delta C_j(\mathbf{r}, \tau) \quad (15)$$

$$\phi_{jjj}(\mathbf{r}_1, \mathbf{r}_2, \mathbf{r}_3, 0, 0) = \bar{C}_j \delta(\mathbf{r}_2 - \mathbf{r}_1) \delta(\mathbf{r}_3 - \mathbf{r}_2) \quad (16)$$

where D_j is the diffusion constant for species j . The boundary condition can be understood by considering eq 13 in the limit of zero delay time and zero displacement ($\mathbf{r}_1 = \mathbf{r}_2 = \mathbf{r}_3$):

$$\phi_{jjj}(\mathbf{r}_1, \mathbf{r}_1, \mathbf{r}_1, 0, 0) = \langle (\delta C_j(\mathbf{r}_1, t))^3 \rangle \quad (17)$$

This limit is equivalent to the third central moment of the distribution of $\delta C_j(\mathbf{r}, t)$. For an ideal dilute sample with negligible intermolecular interactions, $C_j(\mathbf{r}, t)$ is assumed to be well described by a Poisson distribution. The third central moment of a Poisson distribution is equal to the mean, \bar{C} :

$$\sum_{n=0}^{\infty} (n - \bar{C})^3 \frac{\bar{C}^n e^{-\bar{C}}}{n!} = \bar{C} \quad (18)$$

Combining eqs 14, 15, and 16, a solution (Supporting Information) is found for ϕ_{jjj}

$$\begin{aligned} \phi_{jjj}(\mathbf{r}_1, \mathbf{r}_2, \mathbf{r}_3, \tau_1, \tau_2) \\ = \frac{\bar{C}_j e^{-(\mathbf{r}_2 - \mathbf{r}_1)^2 / 4D_j \tau_1} e^{-(\mathbf{r}_3 - \mathbf{r}_2)^2 / 4D_j (\tau_2 - \tau_1)}}{64\pi^3 D_j^3 \tau_1^{3/2} (\tau_2 - \tau_1)^{3/2}} \end{aligned} \quad (19)$$

Correlations interpreted with models that use the Markov assumption require delay time ordering $0 \leq \tau_1 \leq \tau_2$ to preserve the temporal sequence of the observations. Strictly speaking, this inequality restricts correlations to a triangular domain of positive τ_1 and τ_2 values. To simplify both the calculation and presentation of triple correlation data, they are later presented over a square domain where points in the range $\tau_1 > \tau_2$ are interpreted by mapping to a correlation obtained with the last two channels swapped:

$$G_{\alpha \times \beta \times \gamma}(\tau_1, \tau_2) \rightarrow G_{\alpha \times \gamma \times \beta}(\tau_2, \tau_1); \quad \tau_1 > \tau_2 \quad (20)$$

This theory can be expanded to treat interconverting species by rewriting eq 15 as a linear system of reactions and providing the appropriate rates and initial conditions. This would allow investigation of chemical reactions on the time-scale of diffusion, such as intermolecular conformational changes and

the fast intermolecular reactions that provided the initial motivation for double correlation FCS.⁹ Such kinetics would be of considerable interest given the ability of F3CS to resolve reactions using two distinct delay times τ_1, τ_2 .

Solution of the Single-Species Triple FCS Equation.

Before eq 12 is solved for $G_{jjj}(\tau_1, \tau_2)$, the microscope excitation and detection geometry must be modeled. For single-photon excitation, an analytical solution for $G_{jjj}(\tau_1, \tau_2)$ is found if the microscope point-spread function $I(\mathbf{r})$ is assumed to be a Gaussian ellipsoid with $1/e^2$ radius r_0 normal to the focal plane and z_0 orthogonal to the focal plane.

$$I(\mathbf{r}) = \left(\frac{2}{\pi}\right)^{3/2} \frac{1}{r_0^2 z_0} e^{-2(r_x^2 + r_y^2)/r_0^2} e^{-2r_z^2/z_0^2} \quad (21)$$

$$\int I(\mathbf{r}) d\mathbf{r} = 1$$

The function is normalized to unity for convenience. This approximation has been successfully applied to double correlation FCS, and deviations from ideality are well-studied for various excitation schemes and detection geometries.³⁴

With known functional forms for $I(\mathbf{r})$ and $\phi_{jjj}(\mathbf{r}_1, \mathbf{r}_2, \mathbf{r}_3, \tau_1, \tau_2)$, $G_{jjj}(\tau_1, \tau_2)$ can now be written explicitly and solved (Supporting Information)

$$\begin{aligned} G_{jjj}(\tau_1, \tau_2) &= \frac{\bar{C}_j}{\pi^3 r_0^4 z_0^2} \left(\frac{4}{3}\right)^{3/2} \\ &\times (1 + 4\tau_1(\tau_2 - \tau_1)/3\tau_D^2 + 4\tau_2/3\tau_D)^{-1} \\ &\times (1 + 4\tau_1(\tau_2 - \tau_1)/3\omega^4 \tau_D^2 + 4\tau_2/3\omega^2 \tau_D)^{-1/2} \end{aligned} \quad (22)$$

where $\tau_D = r_0^2/4D_j$ and $\omega = z_0/r_0$. Equation 22 also has a role as an intermediate expression in time-integrated fluorescence cumulant analysis,⁷ where even though high-order correlation functions are not directly detected, their treatment of diffusion improves theoretical models that fit fluorescence cumulants collected with long sampling times. Solutions of eq 22 for multiphoton excitation are detailed in the Supporting Information.

Concentrations, Focal Volumes, and Numbers of Molecules. The amplitude of the zero-delay limit of eq 11 is reached by combining eqs 12 and 16:

$$\begin{aligned} G_{\alpha \times \beta \times \gamma}(\tau_1 \rightarrow 0, \tau_2 \rightarrow 0) \\ = \left[\int I^3(\mathbf{r}_1) d\mathbf{r}_1 \right] \frac{\sum_{j=1}^M \varepsilon_{\alpha,j} \varepsilon_{\beta,j} \varepsilon_{\gamma,j} \bar{C}_j}{\langle i_{\alpha}(t) \rangle \langle i_{\beta}(t) \rangle \langle i_{\gamma}(t) \rangle} \end{aligned} \quad (23)$$

The amplitude is a function of the molar concentrations of analyte, \bar{C}_j , but FCS data are more naturally analyzed in terms of the average number of molecules occupying the microscope focal volume, \bar{N}_j . For both double correlation FCS and F3CS, converting from concentration to numbers of molecules is simply a matter of multiplying the concentrations with the effective focal volume of the microscope ($\bar{N}_j = V_{\text{eff}} \bar{C}_j$), but this volume differs between double and triple correlation FCS. The effective volume is not a true volume but a contrast ratio with units of length cubed, and while the effective volume scales linearly with the size of the focal volume, it also depends on the shape. The focal volume relations developed for high-order correlations^{19,22} are used to calculate the double and triple effective volumes, $^2V_{\text{eff}}$ and $^3V_{\text{eff}}$, respectively (alternately

referred to as gamma factors $1/\gamma_n^{9,22}$)

$$^2V_{\text{eff}} = \frac{1}{\gamma_2} = \frac{[\int I(\mathbf{r}) \, d\mathbf{r}]^2}{\int I^2(\mathbf{r}) \, d\mathbf{r}} \quad (24)$$

$$(^3V_{\text{eff}})^2 = \frac{1}{\gamma_3} = \frac{[\int I(\mathbf{r}) \, d\mathbf{r}]^3}{\int I^3(\mathbf{r}) \, d\mathbf{r}} \quad (25)$$

The corresponding numbers of molecules are $^2\bar{N}_j = ^2V_{\text{eff}}\bar{C}_j$ for double correlations and $^3\bar{N}_j = ^3V_{\text{eff}}\bar{C}_j$ for triple correlations. Formally, the conversion of eq 23 from \bar{C}_j to \bar{N}_j proceeds by rescaling the molecular brightness terms $\varepsilon_{\alpha,j}$, which were earlier defined in terms of photons per molar concentration but are now rewritten in terms of photons per number of molecules $^3Y_{\alpha,j}$ (kHz/molecule)

$$^3Y_{\alpha,j} = \gamma_3^{1/2} \varepsilon_{\alpha,j} \int I(\mathbf{r}) \, d\mathbf{r}$$

such that

$$\langle i_{\alpha}(t) \rangle = b_{\alpha} + \sum_{j=1}^M ^3Y_{\alpha,j} ^3\bar{N}_j \quad (26)$$

When $G(0,0)$ is rewritten in terms of $^3Y_{\alpha,j}$, the effective volumes fall out and concentrations are converted to numbers of molecules.

$$\begin{aligned} G_{\alpha \times \beta \times \gamma}(0, 0) &= ^3V_{\text{eff}} \frac{\sum_{j=1}^M ^3Y_{\alpha,j} ^3Y_{\beta,j} ^3Y_{\gamma,j} \bar{C}_j}{\langle i_{\alpha}(t) \rangle \langle i_{\beta}(t) \rangle \langle i_{\gamma}(t) \rangle} \\ &= \frac{\sum_{j=1}^M ^3Y_{\alpha,j} ^3Y_{\beta,j} ^3Y_{\gamma,j} ^3\bar{N}_j}{\langle i_{\alpha}(t) \rangle \langle i_{\beta}(t) \rangle \langle i_{\gamma}(t) \rangle} \end{aligned} \quad (27)$$

Combining eq 22 and eq 27, the full $G(\tau_1, \tau_2)$ expression is written similarly

$$\begin{aligned} G_{\alpha \times \beta \times \gamma}(\tau_1, \tau_2) &= \frac{\sum_{j=1}^M ^3Y_{\alpha,j} ^3Y_{\beta,j} ^3Y_{\gamma,j} ^3\bar{N}_j M(\tau_1, \tau_2)}{\langle i_{\alpha}(t) \rangle \langle i_{\beta}(t) \rangle \langle i_{\gamma}(t) \rangle} \end{aligned} \quad (28)$$

$$\begin{aligned} M(\tau_1, \tau_2) &= (1 + 4\tau_1(\tau_2 - \tau_1)/3\tau_D^2 + 4\tau_2/3\tau_D)^{-1} \\ &\times (1 + 4\tau_1(\tau_2 - \tau_1)/3\omega^4\tau_D^2 + 4\tau_2/3\omega^2\tau_D)^{-1/2} \end{aligned}$$

If triple correlation measurements are performed alone, it is convenient to use units of $^3\bar{N}_j$, but if double and triple correlations are used together, they can both be written in terms of $^2\bar{N}_j$ to allow double and triple correlation data to be fit globally

$$G_{\alpha \times \beta}(\tau) = \frac{\sum_{j=1}^M ^2Y_{\alpha,j} ^2Y_{\beta,j} ^2\bar{N}_j M(\tau)}{\langle i_{\alpha}(t) \rangle \langle i_{\beta}(t) \rangle} \quad (29)$$

$$\begin{aligned} G_{\alpha \times \beta \times \gamma}(\tau_1, \tau_2) &= \left(\frac{\gamma_3}{\gamma_2^2} \right) \frac{\sum_{j=1}^M ^2Y_{\alpha,j} ^2Y_{\beta,j} ^2Y_{\gamma,j} ^2\bar{N}_j M(\tau_1, \tau_2)}{\langle i_{\alpha}(t) \rangle \langle i_{\beta}(t) \rangle \langle i_{\gamma}(t) \rangle} \end{aligned} \quad (30)$$

$$\begin{aligned} ^2Y_{\alpha,j} &= \gamma_2 \varepsilon_{\alpha,j} \int I(\mathbf{r}) \, d\mathbf{r} \\ \langle i_{\alpha}(t) \rangle &= b_{\alpha} + \sum_{j=1}^M ^2Y_{\alpha,j} ^2\bar{N}_j \end{aligned}$$

The ratio γ_3/γ_2^2 was calculated numerically for a variety of point-spread functions³⁵ (Supporting Information, Table S1) and determined analytically for a Gaussian point-spread function:

$$\frac{\gamma_3}{\gamma_2^2} = \left(\frac{4}{3} \right)^{3/2} \quad (31)$$

In practice, this ratio must be experimentally determined.

Simple Properties of Triple Correlation Functions.

Equation 27 is simplified by considering an ideal experiment with zero background and one species.

$$G_{\alpha \times \beta \times \gamma}(0, 0) = \frac{^3Y_{\alpha,j} ^3Y_{\beta,j} ^3Y_{\gamma,j} ^3\bar{N}_j}{(^3Y_{\alpha,j} ^3\bar{N}_j)(^3Y_{\beta,j} ^3\bar{N}_j)(^3Y_{\gamma,j} ^3\bar{N}_j)} = \frac{1}{^3\bar{N}_j^2} \quad (32)$$

This relationship between amplitude and N can be thought of intuitively as

$$G(0, 0) = \frac{\langle \delta^3N(t) \delta^3N(t) \delta^3N(t) \rangle}{^3\bar{N}^3} = \frac{^3\bar{N}}{^3\bar{N}^3} = \frac{1}{^3\bar{N}^2}$$

using the Poisson distribution relationship developed earlier (eq 18). Experimental comparisons with double correlations confirm that both the $1/N^2$ dependence and the functional form of eq 29 are correct as written for a Gaussian beam profile and complete validation studies are being reported elsewhere.

High order autocorrelations are a subset of triple correlation data, though a subset that is excluded for experimental reasons. They are obtained in the limit $\tau_1, \tau_2 \rightarrow \tau$

$$\begin{aligned} G(\tau, \tau) &= G_{1,2}(-\tau) \\ &= ^3\bar{N}^{-2} (1 + 4\tau/3\tau_D)^{-1} \\ &\times (1 + 4\tau/3\omega^2\tau_D)^{-1/2} \end{aligned} \quad (33)$$

which agrees with the relations developed by Palmer and Thompson to analyze 2-D Gaussian focal volumes¹⁹ if N -independent portions of their 2-D Gaussian equation are raised to the $3/2$ power.

A Numerical Triple Correlation Architecture Based on the Schätzel Multiple-Tau Scheme. Double and triple correlation integrals are calculated from raw fluorescence intensities with sum-based versions of eqs 1 and 3

$$G_{\alpha \times \beta}(\tau) = \frac{\sum_{d=0}^{T-1} \delta i_{\alpha}(0; d t_Q) \delta i_{\beta}(\tau; d t_Q - \tau)}{T \langle i_{\alpha}(0) \rangle \langle i_{\beta}(\tau) \rangle} \quad (34)$$

$$\begin{aligned} G_{\alpha \times \beta \times \gamma}(\tau_1, \tau_2) &= \frac{\sum_{d=0}^{T-1} \delta i_{\alpha}(0; d t_Q) \delta i_{\beta}(\tau_1; d t_Q - \tau_1) \delta i_{\gamma}(\tau_2; d t_Q - \tau_2)}{T \langle i_{\alpha}(0) \rangle \langle i_{\beta}(\tau_1) \rangle \langle i_{\gamma}(\tau_2) \rangle} \end{aligned} \quad (35)$$

$$\delta i_x(\tau; d t_Q) = i_x(d t_Q) - \langle i_x(\tau) \rangle$$

$$\langle i_x(\tau) \rangle = \frac{1}{T} \sum_{d=0}^{T-1} i_x(d t_Q - \tau)$$

where intensity data $i(t_d)$ are binned with time quantum t_Q such that t_d and delay times τ , τ_1 , and τ_2 are all integer multiples of t_Q . The sign of τ is flipped to facilitate memory access during computation, but if desired, the true $+\tau$ correlation can be computed by first reversing the time order of data. Symmetric normalization³⁶ is used in the denominator to calculate average intensities over the range $-\tau \leq t_d < (Tt_Q - \tau)$ instead of $0 \leq t_d < Tt_Q$ to improve accuracy at large lag times. Numerical evaluation of the triple correlation functions at each time-point t_d requires three sets of data: one zero delay $\delta i(t_d)$, one set of data delayed at multiple values of τ_1 , $\{\delta i(t_d - \tau_1[0]), \delta i(t_d - \tau_1[1]), \dots\}$, and one set of data delayed at multiple values of τ_2 , $\{\delta i(t_d - \tau_2[0]), \delta i(t_d - \tau_2[1]), \dots\}$. To illustrate how this calculation might proceed numerically, the arrays containing this data are represented as adjointed rectangles in Figure 2A.

For FCS with nano- to microsecond time resolution (presently, $t_Q = 800$ ns), there are on the order of $T = 10^8$ – 10^{11} data points per channel, and so evaluating eq 35 for every pair of delay times τ_1 , τ_2 is computationally infeasible. It would also provide unneeded time resolution at long lag times. For example, few experiments require a series of delay times in the 100 ms range that each differ by 1 μ s, although two uncommon exceptions are treated below.

An approximate, discrete correlation function must replace eq 35 and balance computation time with accuracy and time resolution. For double correlations, the Schätzel multiple-tau scheme^{36–38} is a clever solution which has been employed in correlation hardware for decades. In this scheme, the term multiple refers to multiple delay time values $\tau[0]$, $\tau[1]$, $\tau[2]$, ..., not multiple delay time dimensions $\tau_1[0]$, $\tau_2[0]$, $\tau_3[0]$, Before describing the application to triple correlations, it is helpful to illustrate how the multiple-tau scheme enables rapid calculation of double correlations.

The data structure of the multiple-tau correlation scheme bins portions of data to speed up calculations dramatically (Figure 2B). Delayed data are placed in increasingly large bins as $\tau[i]$ increases, such that the mean delay times for each bin form a pseudologarithmic series that spans a large range of delay times with few points

$$\tau[i] = \{0, 1, 2, \dots, 2n, 2(n+1), \dots, 2^j n, 2^j(n+1), \dots, 2^p(n-1)\} \quad (36)$$

Given minimum and maximum desired values of τ , the number of delay time values $\tau[i]$ that span the range depends on the choice of n , which for convenience is always a power of 2. Every n times the delay times increase, the number of data points per bin increases by a factor of 2, up to the maximum bin size of 2^p . Thus, calculations employing larger values of n take longer to calculate but yield correlations with finer time resolution. For double correlation FCS in this work, $n = 32$ and $p = 13$.

When binned, delayed data $\delta i_\beta(t_d - \tau)$ are used to calculate a double correlation (Figure 2C); they are multiplied against identically binned, undelayed data $\delta i_\alpha(t_d)$ to form a Schätzel multiple-tau (sm τ) correlation integral:

$$G_{\alpha \times \beta}^{\text{sm}\tau}(\tau) = \frac{1}{2^j T \langle i_\alpha(0) \rangle \langle i_\beta(\tau) \rangle} \times \sum_{h=0}^{T/2^j-1} \left[\left(\sum_{k=0}^{2^j-1} \delta i_\alpha(0; (2^j h + k)t_Q) \right) \times \left(\sum_{k=0}^{2^j-1} \delta i_\beta(\tau; (2^j h + k)t_Q - \tau) \right) \right] \quad (37)$$

This binning of zero-delay data allows a fast fractal integration scheme, since data binned 2^n times are only used every 2^n loops, further accelerating the calculation (Figure 2D).

Triple correlation data are most useful when evaluated over a set of τ_1 and τ_2 values (shaded rectangles, Figure 2E) that form an evenly spaced grid when viewed on a log–log–linear plot. This domain allows 2-D slices of 3-D triple correlation data to be directly compared with double correlation data. Correlations are calculated over this domain using one zero-delay structure $\delta i_\alpha(t_d)$ (inset, Figure 2E) and two delayed structures $\delta i_\beta(t_d - \tau_1)$ and $\delta i_\gamma(t_d - \tau_2)$ (horizontal and vertical data structures, Figure 2E). However, the price of choosing this domain is that triple correlation integrals cannot be calculated in a true fractal manner. A more complex set of sums is required to preserve fast time resolution in τ_2 when τ_1 is large, and vice versa

$$G_{\alpha \times \beta \times \gamma}^{\text{sm}\tau}(\tau_1, \tau_2) = \frac{1}{2^{j+\omega} T \langle i_\alpha(0) \rangle \langle i_\beta(\tau_1) \rangle \langle i_\gamma(\tau_2) \rangle} \times \sum_{h=0}^{T/2^\omega-1} \left[\sum_{k=0}^{2^\omega-1} \left[\left(\sum_{l=0}^{2^j-1} \delta i_\alpha(0; (2^\omega h + 2^j k + l)t_Q) \right) \times \left(\sum_{l=0}^{2^j-1} \delta i_\beta(\tau_1; (2^\omega h + 2^j k + l)t_Q - \tau_1) \right) \right] \times \left(\sum_{k=0}^{2^\omega-1} \delta i_\gamma(\tau_2; (2^\omega h + k)t_Q - \tau_2) \right) \right]; \quad \omega \geq j \quad (38)$$

Here, ω and j are bin sizes for delay times τ_2 and τ_1 , respectively, and the inequality $\omega \geq j$ forces the ordering of delay times $\tau_1 \leq \tau_2$. Correlation data are calculated for $\tau_1 \geq \tau_2$ by swapping the two delayed data structures.

For both double and triple correlations, the multiple-tau method approximates $G(\tau)$ and $G(\tau_1, \tau_2)$ as weighted averages of exact correlations calculated over a range of local τ or (τ_1, τ_2) values. The weight functions that relate exact triple correlation integrals and multiple-tau integrals are pyramidal in shape and are detailed in the Supporting Information. The effects of the average on double correlation data are illustrated for an arbitrary, rapidly changing function which is averaged using increasingly large bin sizes (Figure 2F). When an arbitrary triple correlation function (Figure 2G) is averaged using increasingly large bins (Figure 2H,I), the amplitude of the center peak decreases rapidly as the bin size increases. Such dramatic effects are not observed in practice, since FCS data rarely decay as quickly as these arbitrary functions.

For two specific instances where it is not desirable that the multiple-tau approximation decreases time resolution at larger delay times, the data analysis protocol can be modified. In the first scenario, if fine-scale time resolution is required at a specific pair of large lag times, two of the three input data streams are time-shifted by these specific lag times prior to calculating the correlation integrals. A more complicated situation occurs in the second scenario, where correlations around the region surrounding the diagonal $G_{\alpha \times \beta \times \gamma}(\tau^*, \tau^* + \delta\tau)$, $\tau^* \gg \delta\tau$ are blurred because the correlation function changes rapidly around $\delta\tau = 0$. This information is actually present with fine-scale time resolution in the permuted correlation $G_{\gamma \times \alpha \times \beta}(-\tau^*, -\delta\tau)$, and thus, a particularly rich data set is the collection of all three unique correlations, each computed with positive and negative delay times. These six correlation curves can be globally fit using a model that takes the pyramidal average into account or simply discards data along the $\tau_1 = \tau_2$ line.

The two- τ multiple- τ scheme outlined here is useful in a wide variety of applications as a rapid way to explore correlations

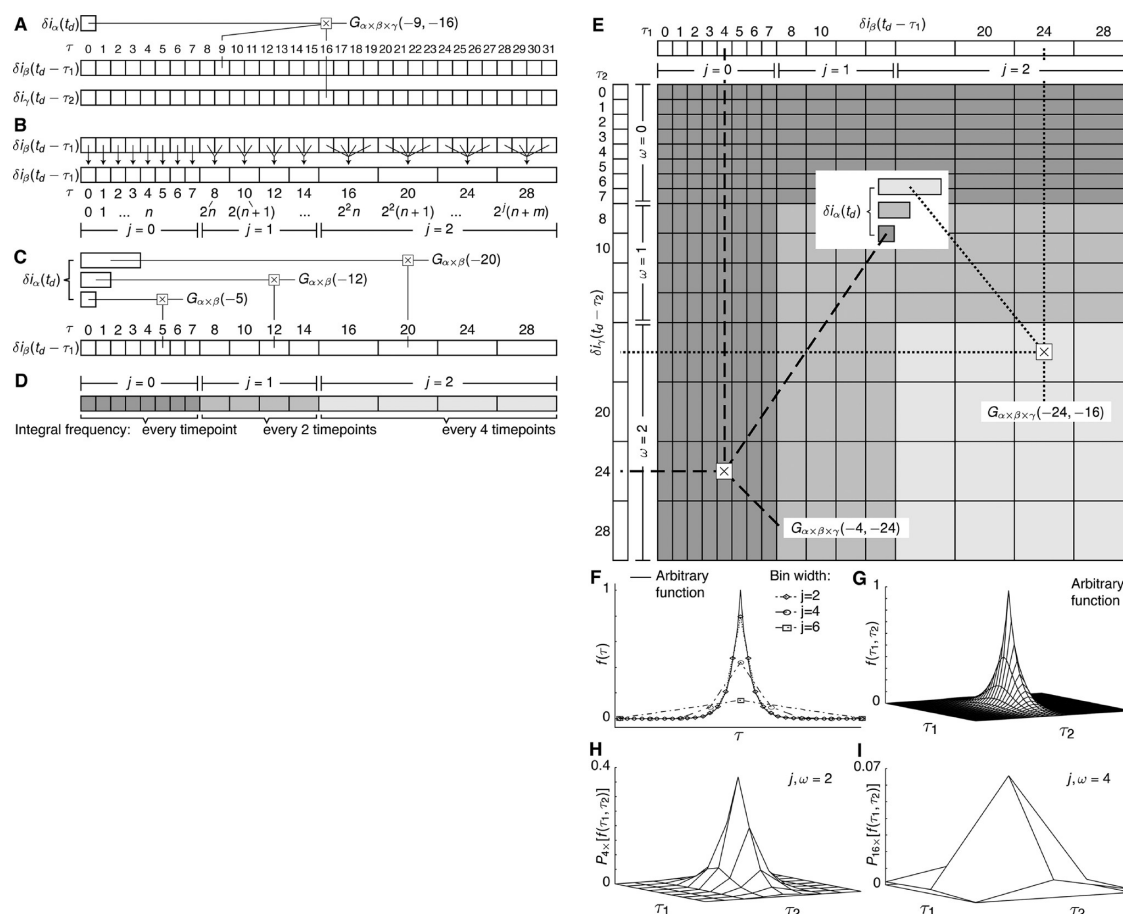


Figure 2. The Schätzel multiple-tau scheme for calculating double correlations is expanded for triple correlations with two dimensions of multiple taus. (A) The simplest data structure required to calculate $G_{\alpha \times \beta \times \gamma}(-\tau_1, -\tau_2)$. Data are represented as adjoined squares. For each time point t_d , one datum of $\delta i_\alpha(t_d)$ and multiple data of $\delta i_\beta(t_d - \tau_1)$ and $\delta i_\gamma(t_d - \tau_2)$ are required. The algorithm loops once per time point, and data are updated before calculations are made. (B) The data structure of the multiple-tau correlation scheme^{36–38} bins data to dramatically speed up calculations. Delayed data are binned by a factor of 2^j , where j is an integer that increases every n data bins after the first $2n$. As a result, the bins' average delay times form a pseudologarithmic series which concisely spans a large range of τ values. (C) A double correlation integral calculated with binned data. $\delta i_\alpha(t_d)$ is also binned to match the size of the delay data. (D) Summands representing larger τ values do not need to be calculated at every loop, further reducing computation time. (E) Multiple-tau principles (B–D) applied to triple correlations. The correlation calculated for each pair of τ_1, τ_2 values is represented as a shaded rectangle. Each correlation sums the triple product of delayed data $\delta i_\beta(t_d - \tau_1)$ and $\delta i_\gamma(t_d - \tau_2)$ and zero-delay data $\delta i_\alpha(t_d)$ (inset). To preserve time resolution, the bin width of zero-delay data is the minimum of the delayed bin widths, 2^j or 2^0 . The shade of each data point indicates the calculation frequency, as before. Multiple-tau methods calculate a weighted average of exact integrals over a region of delay times spanning twice the bin width; this blurs the time resolution. (F) Blurring of an arbitrary, rapidly changing exact double correlation function analyzed with varying bin-widths. (G) A rapidly changing triple correlation function analyzed with multiple bin widths (H, I). The amplitude of the center peak decreases rapidly as binning increases.

over a very large number of time-scales. Triple correlations have been computed for immobilized single enzymes,²⁷ and triple correlations and bispectra have had diverse applications in radio and visible astronomy, oceanography, signal reconstruction, measuring coherence,³⁹ and complex optics.⁴⁰ In these previous cases, correlations have been calculated over linear τ_1 and τ_2 domains, not the logarithmic domains that allow routine FCS experiments to analyze kinetics over 5 or more orders of magnitude. Unlike linear domains, the double logarithmic domain required for F3CS is not easily calculated with Fourier methods. As an alternative to the multiple-tau technique, photon-pair correlation techniques for double correlation integrals are much faster than multiple-tau methods for low count rate samples.⁴¹ Nevertheless, multiple-tau methods were adapted for triple correlations instead because photon-pair techniques become dramatically less efficient than multiple-tau schemes at higher count rates (~ 100 kHz),⁴¹ require

prohibitively higher bandwidth in the data acquisition process, and are awkward to convert to analyze $\delta i(t)$ instead of $i(t)$.

Three-Channel Correlation Avoids Detection Artifacts.

Triple autocorrelation of a single signal $i(t)$ reveals a great deal of information about a system, but the signal can also contain optoelectronic artifacts that are eliminated with a modified experimental setup. This is demonstrated using a biological system, fluorescently labeled 16S rRNA (Figure 3A), which also demonstrates that F3CS can work with biological samples labeled with common fluorophores. The rRNA forms both the structural and functional core of *E. coli* 30S ribosomes,⁴² and to do this, it adopts a remarkably compact and twisted fold.^{43,44} How this fold is achieved is an open question. The rRNA is synthesized as a linear polymer and achieves a compact final shape only after navigating a complex assembly landscape of protein binding and rRNA folding events.⁴⁵ Both protein addition and rRNA folding can in principle be monitored by FCS via changes in the diffusion constant.^{46,47}

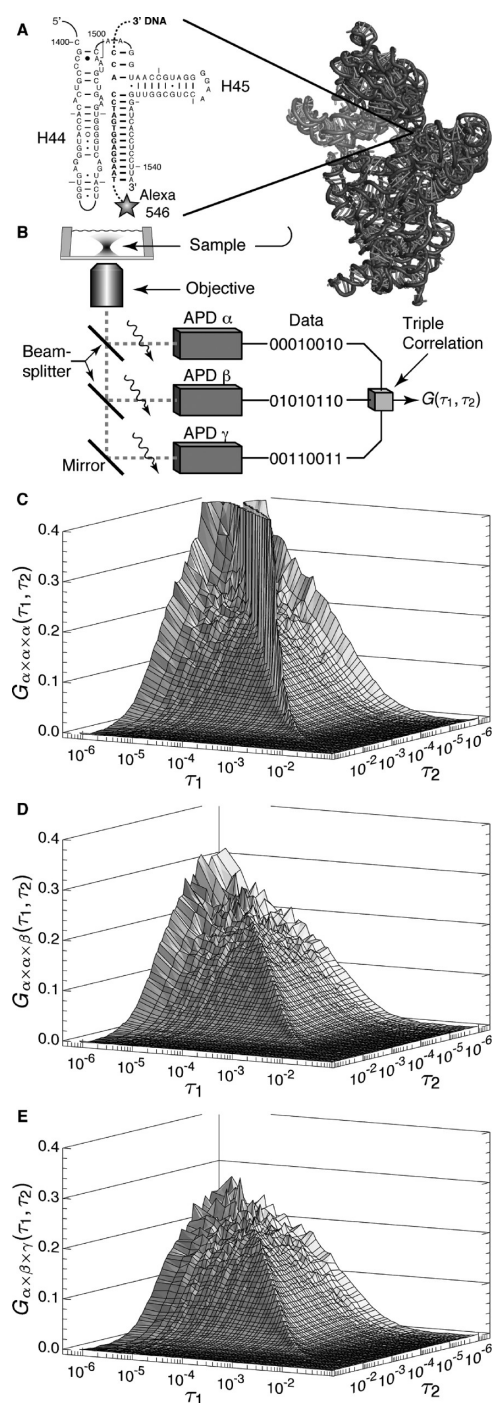


Figure 3. Artifacts in triple correlations are eliminated with three-channel data acquisition. (A) 16S rRNA^{43,42} was fluorescently labeled by annealing a short DNA oligo to the 3' end. The oligo was 5' labeled with the fluorophore Alexa 546. (B) Schematic of the optical system used to collect fluorescence from 16S rRNA. Two beamsplitters split fluorescence across three independent photon detectors (APDs) that are read simultaneously. (C) The correlation curve calculated with signals from detector α only is denoted $G_{\alpha \times \alpha \times \alpha}(\tau_1, \tau_2)$ and contains two sets of decays: slower decays at $\tau_1 = 100 \mu\text{s}$ or $\tau_2 = 100 \mu\text{s}$ result from diffusion of the 16S rRNA in and out of the focal volume, while faster decays at $\tau_1 = 1 \mu\text{s}$ or $\tau_2 = 1 \mu\text{s}$ result from APD after-pulsing, an electronic artifact which routinely complicates double correlation FCS.⁴⁸ (D) The correlation curve obtained using detector α twice and detector β once, $G_{\alpha \times \alpha \times \beta}(\tau_1, \tau_2)$, is free of after-pulsing at short τ_2 . (E) The correlation curve calculated with signals from three independent detectors, $G_{\alpha \times \beta \times \gamma}(\tau_1, \tau_2)$, is free of opto-electronic artifacts.

The fluorescence intensity is split evenly among three detectors, α , β , and γ (Figure 3B). A triple autocorrelation function calculated solely with one signal ($G_{\alpha \times \alpha \times \alpha}(\tau_1, \tau_2)$) (Figure 3C) contains several decays. The decays around $100 \mu\text{s}$ to 1 ms are expected from diffusion of a compacted 16S rRNA, but the ridge-line along $\tau_1 = \tau_2$ and the shoulders where $\tau_1 < 5 \mu\text{s}$ or $\tau_2 < 5 \mu\text{s}$ are due to the photon detector artifact after-pulsing, a false photon detection event occurring within a few microseconds of a legitimate photon detection (reviewed in ref 48). As expected, after-pulsing was also detected in double autocorrelations from the same time traces.

The three independent channels in Figure 3B report the same correlated molecular events, but there is no correlation between after-pulsing events on different detectors. Thus, the two-channel correlation ($G_{\alpha \times \alpha \times \beta}(\tau_1, \tau_2)$) (Figure 3D) loses two of the three after-pulsing spikes, and three-channel data $G_{\alpha \times \beta \times \gamma}(\tau_1, \tau_2)$ (Figure 3E) lack after-pulsing entirely. Three-channel data are free of any obvious artifacts in general.

The same autocorrelation data that exhibit after-pulsing also contain additional correlation amplitudes along three regions where triple correlation and high-order correlation $G_{1,2}(\tau)$ integrals overlap: $G(\tau, 0)$, $G(0, \tau)$, and $G(\tau, \tau)$ (outside of the plot range of Figure 3C). The amplitudes result from statistics of random photon detection that can normally be ignored in double correlation FCS but affect high-order correlation data and must be corrected for.²² The correlation is inescapable in microscopes that do not collect the majority of photons, and is exacerbated by lower-concentration samples and faster time resolutions. As with after-pulsing, detection with three independent channels eliminates this additional correlation amplitude.

Three-channel detection does have disadvantages, namely, an increase in experimental complexity and reduced data quality from splitting the signal. However, data quality is mostly recovered by averaging together all three pairs of unique correlations, and three-channel detection allows clean data to be collected with avalanche photodiodes (APDs), which are fast and sensitive photon counters. Experiments using different detectors, such as the CCD-based system employed by Edman et al. for immobilized triple correlation analysis,²⁷ are not subject to after-pulsing but lose orders of magnitude of time resolution. On the whole, the use of three-channel detection to calculate a triple autocorrelation is a compromise but a good one.

Error Estimates and Data Quality in F3CS. The precision to which triple correlation data are calculated is determined by the interplay of correlation architecture, optics, dye photophysics, and basic experimental parameters such as acquisition time. The strong influence of correlation architecture on the shape of the error profile is seen in experimental error estimates (Figure 4A) for the triple correlation of a random light source. Error estimates vary with delay times, with the least precise data describing fast events at short lag times. Correlation data become more precise as τ_1 and/or τ_2 increases.

The waterfall shape of Figure 4A is accurately modeled (Figure 4B) by considering the number of raw data points that contribute to each correlation estimate. Because of the pseudo-logarithmic τ series introduced earlier, every n th time τ_1 or τ_2 increases, the τ bin width doubles and twice as much data are used, resulting in a $\sqrt{2}$ reduction in error. Error is reduced at the expense of time resolution by setting up correlation integrals with a smaller value of n such that more data are used to compute each correlation point (data for the first $2n$ values of $\tau_{1,2}$ remain unaffected). In general, data calculated with smaller n are

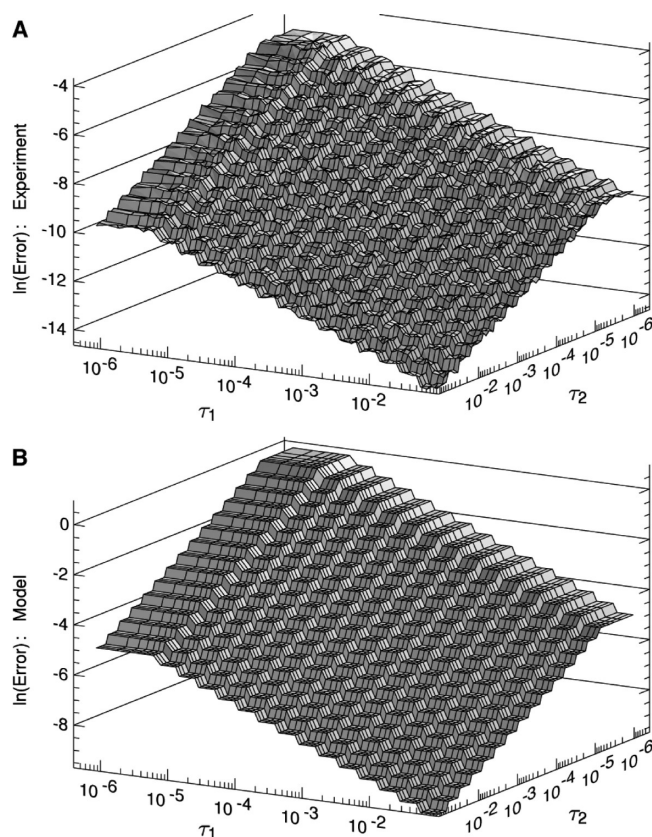


Figure 4. Delay times and correlation architecture affect the precision to which each triple correlation data point is calculated. (A) Experimental error is estimated as the standard deviation of the zero-valued correlation curve obtained by correlating a quasi-random light source. The waterfall pattern occurs because the number of data points used to calculate each point increases as either τ_1 and/or τ_2 increases, and integrating over more data improves each estimate. (B) The shape of the error estimate is accurately modeled as a $\sqrt{2}$ reduction in error for each 2-fold increase in the number of data points averaged. A result of the error plot is that $G(0,0)$ values are better estimated using F3CS rather than coincidence methods.²⁶ Coincidence data are equivalent to the single F3CS data point at $\tau_1 = \tau_2 = 0$, which is one of the least precise data points in the entire F3CS data set. In contrast, F3CS data estimate $G(0,0)$ by fitting the entire data set, utilizing a set of multiple data points, each as precise or more precise than the coincidence data point.

more easily interpreted by eye, though the concomitant reduction in the number of data points makes such data less amenable to nonlinear least-squares fitting routines. As with double correlation FCS, the diffusion and reaction of the molecules under analysis also contributes a τ -dependent error term,^{38,49} though this impacts precision to a lesser extent than correlation architecture.

The global magnitudes of errors in both double and triple correlations are determined by count rate, acquisition time, and background signals. The effects of count rate and acquisition time are illustrated in Figure 5A and B, respectively. Both double and triple correlations have a linear dependence on count rate, even though they respectively require pairs and triples of photons. The correlation curve quality increases with the square root of total acquisition time, as expected for a series of independent measurements.

Both observations together mean that double and triple FCS errors are not solely dependent on the total number of photons detected. For experiments where a limited number of photons can be detected (such as in an immobilized FCS experiment⁵⁰), correlation quality is maximized by shorter, brighter time traces.

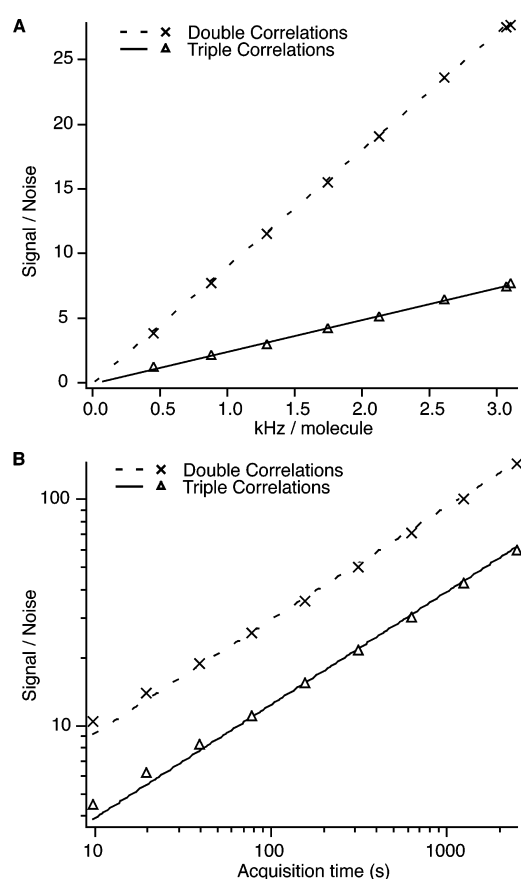


Figure 5. The overall precision of correlation data increases with greater fluorophore brightness and longer acquisition time. (A) Precision of 16S rRNA–Alexa546 data collected with identical excitation conditions but different effective molecular brightnesses obtained by placing neutral density filters in the detection path. Both double and triple correlation data showed a linear dependence of curve quality on count rate. (B) The signal-to-noise of both double and triple correlation data, each as a function of acquisition time, is fit to a line with a slope of 1/2, showing that data quality is proportional to the square-root of acquisition time.

In general, individual triple correlation data points appear less precise than double correlation data points calculated from the same raw photon counts, though again this depends on how the correlation integrals are set up. However, the larger number of data points available for fitting triple correlations, 4096 vs 416 in Figure 5, for example, improve fitting statistics and compensate for noisier individual data points.

Understanding error estimates is essential not just for fitting data with weighted nonlinear least-squares methods and understanding the appearance of primary data but also for designing new instruments experiments. The route to improving triple correlation FCS experiments through brighter fluorophores, maximal excitation conditions, higher photon throughput, and longer acquisition times often requires trade-offs that must be evaluated in terms of signal-to-noise. For example, the 1.45 N.A. oil-immersion objective utilized in this study maximized brightness at the expense of working distance, sensitivity to focal drift, and focal volume quality. Similarly, excitation conditions had to carefully balance the benefits of bright fluorescence with nonlinear effects caused by saturation and photobleaching.

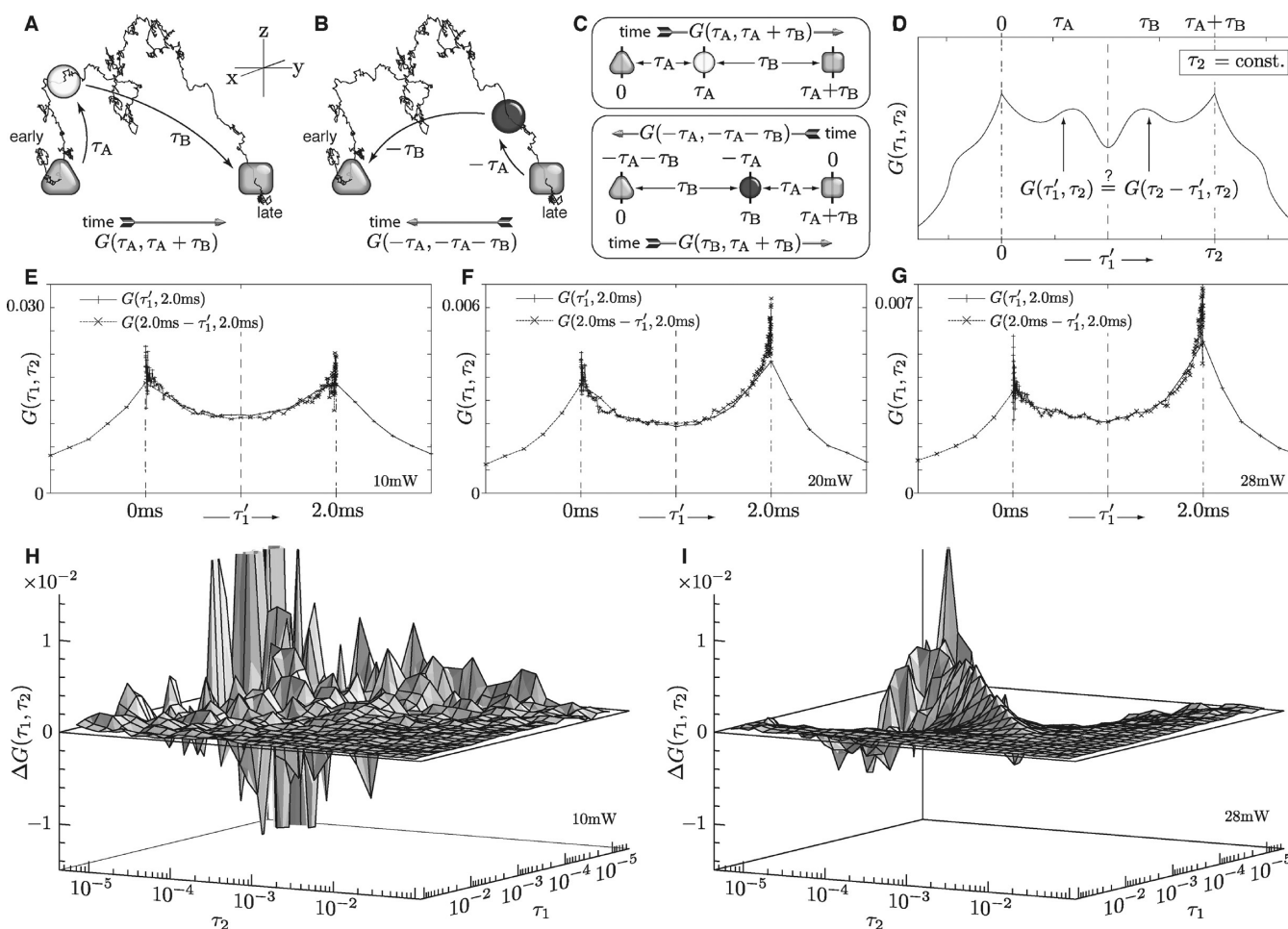


Figure 6. Detecting broken time-reversal symmetry using triple correlation functions. (A) The three observations of a triple correlation $G(\tau_A, \tau_A + \tau_B)$ capture a molecule in three potentially different states (triangle, circle, square) as it diffuses along a trajectory. (B) With triple correlations that go backward in time $G(-\tau_A, -\tau_A - \tau_B)$, the middle observation captures a fourth state (black circle) which can differ from the white circle state, showing that forward and backward correlations of the same data are not necessarily identical.²⁴ While forward and backward triple correlations of reversible processes, such as chemical reaction networks at equilibrium, must be equal, irreversible processes are not so constrained.^{25,23} (C) Timelines depict the order of the observations in parts A and B and illustrate a relation that allows reverse correlations to be rewritten with positive delay times. (D) Using the relation in part C, the presence of time reversal symmetry is equivalent to mirror symmetry in correlation functions $G(\tau_1, \tau_2 = \text{constant})$ about the point $\tau_1 = \tau_2/2$. (E) Experimental proof of mirror symmetry from diffusing 16S rRNA molecules probed with low-intensity laser light. Because of the way correlation integrals are calculated, two overlapping correlation functions $G(\tau_1, \tau_2)$ and $G(\tau_2 - \tau_1, \tau_2)$ are required to provide complete coverage. The functions differ at $\tau_1 = \{0, \tau_2\}$ due to binning and the finely sampled points are more accurate. (F, G) As part E, but mirror symmetry is lost when increasing laser powers cause irreversible photobleaching.²³ The same data are more naturally analyzed as difference correlations $\Delta G(\tau_1, \tau_2) = G(\tau_1, \tau_2) - G(-\tau_1, -\tau_2)$. (H) Difference correlations of the lowest laser power are flat, consistent with a reversible system. (I) Difference correlations of the highest laser power are nonzero, indicating an irreversible system. The shape of the difference correlation characterizes irreversible dynamics over several orders of magnitude in time.

Photobleaching, Irreversible Behaviors, and Symmetries. Triple autocorrelation experiments have been proposed^{23–25,27} as a means to discriminate between reversible and irreversible processes such as equilibrium and nonequilibrium steady-state reaction networks. If reversible processes connect the earliest and latest times, then the forward and backward correlation functions should be identical:

$$G(\tau_A, \tau_A + \tau_B) = \frac{\langle \delta i(t) \delta i(t + \tau_A) \delta i(t + \tau_A + \tau_B) \rangle}{\langle i(t) \rangle^3} \quad (39)$$

$$G(-\tau_A, -\tau_A - \tau_B) = \frac{\langle \delta i(t) \delta i(t - \tau_A) \delta i(t - \tau_A - \tau_B) \rangle}{\langle i(t) \rangle^3} \quad (40)$$

where the subscripts below $i(t)$ have been dropped because the following only applies to identical signals, or as above, independently acquired signals that report the same molecular events in identical ways. Equation 39 correlates molecular behavior at three times, t , $t + \tau_A$, and $t + \tau_A + \tau_B$ (Figure 6A), while eq 40 reverses the order of the observation events (Figure 6B), and is also rewritten in terms of positive delay times (Figure 6C) with the assumption that $i(t)$ is stationary:

$$G(-\tau_A, -\tau_A - \tau_B) = \frac{\langle \delta i(t) \delta(t - \tau_A) \delta i(t - \tau_A - \tau_B) \rangle}{\langle i(t) \rangle^3} = \frac{\langle \delta i(t + \tau_A + \tau_B) \delta i(t + \tau_B) \delta i(t) \rangle}{\langle i(t) \rangle^3} = G(\tau_B, \tau_A + \tau_B) \quad (41)$$

Thus, any difference between $G(\tau_A, \tau_A + \tau_B)$ and $G(\tau_B, \tau_A + \tau_B)$ is evidence of irreversibility in the system^{19–25} and would break mirror symmetry in one-dimensional slices of triple correlation functions $G(\tau_1, \tau_2)$ about the point $\tau_1 = \tau_2/2$ (Figure 6D). This is directly tested with a sample of freely diffusing 16S rRNA examined at multiple laser powers. At low laser power, mirror symmetry is present (Figure 6E). As laser power increases, mirror symmetry is gradually lost (Figure 6F,G). Both observations are consistent with predictions, as the system is reversible at low laser powers, but molecules undergo irreversible photobleaching as laser power increases. At the same powers, photobleaching is independently observed as changes in the apparent τ_D and correlation amplitude in double correlations calculated from the same data (not shown). Irreversible photobleaching has previously been observed with high-order autocorrelations,²³ which are equivalent to the two points in the triple correlation data where $\tau_1 = \{0, \tau_2\}$. With both high-order correlations and F3CS, the amplitude of the correlation signal increases at larger τ_1 and data from later time points are weighted more heavily than data from earlier time points.

The one-dimensional slices of the correlation function in Figure 6E–G are awkward to work with because they require two correlation curves to be overlaid, one of which is computed with negative delay times. Confusingly, the two curves contain different time resolutions at identical τ_1 and different values because they are calculated as weighted averages over different time-scales. A more consistent way to display the whole data set is as a full two-dimensional plot of the difference

$$\Delta G(\tau_1, \tau_2) = G(\tau_1, \tau_2) - G(-\tau_1, -\tau_2) \quad (42)$$

$$= G(\tau_1, \tau_2) - G(\tau_2 - \tau_1, \tau_2) \quad (43)$$

Equation 42 is readily computed, and eq 43 is exactly the equality to be tested for the detection of irreversible systems. The raw data used to compute Figure 6E,G were analyzed with eq 42. Difference data from the low power experiment are zero within error (Figure 6H), with noise at fast delay times as expected. Data collected at high laser power are nonzero, indicating the presence of irreversible reaction (Figure 6I). A few geometric features of the difference curves result in part from equalities derived from eq 5

$$\begin{aligned} \Delta G(\tau, 2\tau) &= 0 = \Delta G(2\tau, \tau) \\ \Delta G(\tau_1, \tau_2) &= \Delta G(\tau_2, \tau_1) \\ \Delta G(\tau, \tau) &= -\Delta G(0, \tau) \end{aligned} \quad (44)$$

but otherwise the shape of $\Delta G(\tau_1, \tau_2)$ contains information about the kinetics and amplitudes of irreversible processes. The $\Delta G(\tau_1, \tau_2)$ relations provide a computationally inexpensive and simple way to search for irreversible reactions over several orders of magnitude in time. For biomolecular reactions and other kinetic processes, the influences of irreversible reactions are modeled by modifying the molecular correlation function $\phi_{jjj}(\mathbf{r}_1, \mathbf{r}_2, \mathbf{r}_3, \tau_1, \tau_2)$ and resolving eq 9 analytically or numerically. Processes that are influenced by laser excitation, such as photobleaching, require more complicated numerical treatment. As the equalities in this section only apply to triple autocorrelation FCS where all input signals record the same process the same way, and no signal preferentially records any molecular state, the equalities do not restrict the ability of F3CS to monitor complex equilibrium kinetics using multiple color detection.

CONCLUSIONS

Time-correlation formalisms play a central role in nonequilibrium statistical mechanics and the theoretical frameworks of many types of optical spectroscopy. FCS is unique in that it provides direct access to molecular correlation functions, minimally unobscured by the interaction between radiation and matter. By introducing a second delay time, F3CS allows a more complex class of molecular correlations to be probed which can examine linked kinetics and the time-reversibility of complex systems. While the development of F3CS was an obvious way to greatly increase the information content of simple fluorescence experiments, several theoretical, numerical, and experimental challenges made implementation nontrivial. With a statistical mechanics framework, numerical triple correlation strategies, and an understanding of the influence of basic spectroscopic and hardware factors on data quality, the much hypothesized spectroscopic technique F3CS is now possible.

ASSOCIATED CONTENT

Supporting Information

Details on the solution of the molecular correlation function, details on the solution of the single-species FCS function, and numerical solutions of the triple correlation function, calculations of effective volumes for double and triple correlations, adjustments for multiphoton spectroscopy, and weight functions relating exact and multiple-tau triple correlations. This material is available free of charge via the Internet at <http://pubs.acs.org>.

AUTHOR INFORMATION

Corresponding Author

*E-mail: jrwill@scripps.edu.

ACKNOWLEDGMENTS

Thanks to M. Talkington for the gift of purified 16S rRNA. W.K.R. appreciates many helpful discussions with S. Y. Berezina, J.-P. Clamme, A. A. Deniz, Z. Shajani, and M. T. Sykes. This work was funded by grants from the National Institutes of Health (R37-GM-53757 to J.R.W., GM-044060 to D.P.M.) and the National Science Foundation (Graduate Research Fellowship to W.K.R.).

REFERENCES

- (1) Qian, H.; Elson, E. L. *Proc. Natl. Acad. Sci. U.S.A.* **1990**, *87*, 5479–5483.
- (2) Qian, H.; Elson, E. L. *Biophys. J.* **1990**, *57*, 375–380.
- (3) Kask, P.; Palo, K.; Ullmann, D.; Gall, K. *Proc. Natl. Acad. Sci. U.S.A.* **1999**, *96*, 13756–13761.
- (4) Kask, P.; Palo, K.; Fay, N.; Brand, L.; Mets, Ü.; Ullmann, D.; Jungmann, J.; Pschorr, J.; Gall, K. *Biophys. J.* **2000**, *78*, 1703–1713.
- (5) Chen, Y.; Müller, J. D.; So, P. T. C.; Gratton, E. *Biophys. J.* **1999**, *77*, 553–567.
- (6) Wu, B.; Chen, Y.; Müller, J. D. *Biophys. J.* **2006**, *91*, 2687–2698.
- (7) Wu, B.; Müller, J. D. *Biophys. J.* **2005**, *89*, 2721–2735.
- (8) Magde, D.; Elson, E.; Webb, W. W. *Phys. Rev. Lett.* **1972**, *29*, 705–708.
- (9) Elson, E. L.; Magde, D. *Biopolymers* **1974**, *13*, 1–27.
- (10) Haustein, E.; Schwill, P. *Annu. Rev. Biophys. Biomol. Struct.* **2007**, *36*, 151–169.
- (11) Digman, M. A.; Gratton, E. *Annu. Rev. Phys. Chem.* **2011**, *62*, 645–668.
- (12) Schwill, P.; Meyer-Almes, F. J.; Rigler, R. *Biophys. J.* **1997**, *72*, 1878–1886.

- (13) Heinze, K. G.; Rarbach, M.; Jahnz, M.; Schwille, P. *Biophys. J.* **2002**, *83*, 1671–1681.
- (14) Book, B.; Chen, J.; Irudayaraj, J. *Biotechnol. Bioeng.* **2011**, *108*, 1222–1227.
- (15) Chen, H.; Farkas, E. R.; Webb, W. W. *Methods Cell Biol.* **2008**, *89*, 3–35.
- (16) Gopich, I. V.; Szabo, A. *J. Phys. Chem. B* **2005**, *109*, 17683–17688.
- (17) Palo, K.; Mets, Ü.; Jäger, S.; Kask, P.; Gall, K. *Biophys. J.* **2000**, *79*, 2858–2866.
- (18) Palo, K.; Mets, Ü.; Loorits, V.; Kask, P. *Biophys. J.* **2006**, *90*, 2179–2191.
- (19) Palmer, A. G.; Thompson, N. L. *Biophys. J.* **1987**, *52*, 257–270.
- (20) Palmer, A. G.; Thompson, N. L. *Proc. Natl. Acad. Sci. U.S.A.* **1989**, *86*, 6148–6152.
- (21) Palmer, A. G.; Thompson, N. L. *Rev. Sci. Instrum.* **1989**, *60*, 624–633.
- (22) Palmer, A. G.; Thompson, N. L. *Appl. Opt.* **1989**, *28*, 1214–1220.
- (23) Melnykov, A. V.; Hall, K. B. *J. Phys. Chem. B* **2009**, *113*, 15629–15638.
- (24) Steinberg, I. Z. *Biophys. J.* **1986**, *50*, 171–179.
- (25) Qian, H.; Elson, E. *Proc. Natl. Acad. Sci. U.S.A.* **2004**, *101*, 2828–2833.
- (26) Heinze, K. G.; Jahnz, M.; Schwille, P. *Biophys. J.* **2004**, *86*, 506–516.
- (27) Edman, L.; Rigler, R. *Proc. Natl. Acad. Sci. U.S.A.* **2000**, *97*, 8266–8271.
- (28) Burkhardt, M.; Heinze, K. G.; Schwille, P. *Opt. Lett.* **2005**, *30*, 2266–2268.
- (29) Bestvater, F.; Seghiri, Z.; Kang, M. S.; Gröner, N.; Lee, J. Y.; Im, K. B.; Wachsmuth, M. *Opt. Express* **2010**, *18*, 23818–23828.
- (30) Talkington, M. W. T.; Siuzdak, G.; Williamson, J. R. *Nature* **2005**, *438*, 628–632.
- (31) Aitken, C. E.; Marshall, R. A.; Puglisi, J. D. *Biophys. J.* **2008**, *94*, 1826–1835.
- (32) Cordes, T.; Vogelsang, J.; Tinnefeld, P. *J. Am. Chem. Soc.* **2009**, *131*, 5018–5019.
- (33) Digman, M. A.; Gratton, E. *Biophys. J.* **2009**, *97*, 665–673.
- (34) Hess, S. T.; Webb, W. W. *Biophys. J.* **2002**, *83*, 2300–2317.
- (35) Richards, B.; Wolf, E. *Philos. Trans. R. Soc. London, Ser. A* **1959**, *253*, 358–379.
- (36) Schätzel, K.; Drewel, M.; Stimac, S. *J. Mod. Opt.* **1988**, *35*, 711–718.
- (37) Schatzel, K. *Inst. Phys. Conf. B* **1985**, *77*, 175–184.
- (38) Schatzel, K. *Quantum Opt.* **1990**, *2*, 287–305.
- (39) Ma, L.; Rakher, M. T.; Stevens, M. J.; Slattery, O.; Srinivasan, K.; Tang, X. *Opt. Express* **2011**, *19*, 10501–10510.
- (40) Lohman, A. W.; Wirnitzer, B. *Proc. IEEE* **1984**, *72*, 889–901.
- (41) Laurence, T. A.; Fore, S.; Huser, T. *Opt. Lett.* **2006**, *31*, 829–831.
- (42) Schuwirth, B. S.; Borovinskaya, M. A.; Hau, C. W.; Zhang, W.; Vila-Sanjurjo, A.; Holton, J. M.; Cate, J. H. D. *Science* **2005**, *310*, 827–834.
- (43) Cannone, J. J.; Subramanian, S.; Schnare, M. N.; Collett, J. R.; D'Souza, L. M.; Du, Y.; Feng, B.; Lin, N.; Madabusi, L. V.; Muller, K. M.; Pande, N.; Shang, Z.; Yu, N.; Gutell, R. R. *BMC Bioinf.* **2002**, *3*, 1471–2105.
- (44) Noller, H. F. *Science* **2005**, *309*, 1508–1514.
- (45) Adilakshmi, T.; Bellur, D.; Woodson, S. *Nature* **2008**, *455*, 1268–1272.
- (46) Hill, W. E.; Bakke, K. R.; Blair, D. P. *Nucleic Acids Res.* **1977**, *4*, 473–476.
- (47) Tam, M. F.; Hill, W. E. *Biochemistry* **1981**, *20*, 6480–6484.
- (48) Zhao, M.; Jin, L.; Chen, B.; Ding, Y.; Ma, H.; Chen, D. *Appl. Opt.* **2003**, *42*, 4031–4036.
- (49) Wohland, T.; Rigler, R.; Vogel, H. *Biophys. J.* **2001**, *80*, 2987–2999.
- (50) Kim, H. D.; Nienhaus, G. U.; Ha, T.; Orr, J. W.; Williamson, J. R.; Chu, S. *Proc. Natl. Acad. Sci. U.S.A.* **2002**, *99*, 4284–4289.